Vertical pore pressure variations and geotechnical sediment properties at a sandy beach

Nina Stark [a,*], Peter Mewis [b], Bridgit Reeve [a], Matthew Florence [a], Jan Piller [b], Jessica Simon [b]

[a] *Virginia Tech, Charles E. Via, Jr., Department for Civil and Environmental Engineering, Blacksburg, USA*
[b] *Technische Universität (TU) Darmstadt, Department of Civil and Environmental Engineering, Darmstadt, Germany*

ARTICLE INFO

ABSTRACT

The role of geotechnical properties and soil behavior for beach dynamics has been recognized before, but geotechnical field measurements in energetic beach environments are still rare. This study focused on two days of field measurements along a cross-shore transect reaching from the foot of the dunes to the upper subtidal zone at the western sandy beach of the island of Sylt, Germany, just south of the city of Westerland. Sediment properties and geotechnical parameters were obtained from sediment sampling and limited in-situ testing. Pore pressure measurements were conducted along a vertical array in the upper 55 cm of the beach surface in the lower intertidal zone. Pore pressure recordings were then analyzed using a one-dimensional-vertical (1DV) model based on Biot (1956) and Mei and Foda (1981). Laboratory testing results demonstrated slight trends of increasing grain size and friction angles from the subaerial to the lower intertidal zone. In-situ sediment strength testing using a portable free fall penetrometer supported the trends in friction angles for the subaerial and intertidal zone. Additionally, a significant increase in sediment resistance was observed in the swash zone and upper subtidal zone. Pore pressure recordings showed a consistent trend associated with the tidal water elevations. However, data collected during low tide suggested a decoupling of surface water effects and groundwater, possibly associated with gas content and negative pore pressures in the vadose zone. Pore pressure recordings also suggested a more pronounced wave damping in the upper sediment layers and a minor phase lag. The 1DV pore pressure model succeeded to simulate the observed pressures at all sediment depths well, and suggested no liquefaction events during the measurement period, but a reduction of effective weight that may affect sediment dynamics.

1. Introduction

Beach erosion is one of the most pressing issues with regards to modern coastline preservation and protection from land loss and is particularly a concern with regard to sea level rise (Bird 1996; Leatherman et al., 2000; Ruggiero et al., 2001; Zhang et al., 2004). Although the importance of geotechnical soil characteristics such as friction angles, cohesion, and pore pressure on erodibility and threshold shear stresses has been recognized (e.g., Kirchner et al., 1990; Turner and Nielsen 1997; Foster et al., 2006; Van Rijn 2007; Grabowski et al., 2011; Stark et al., 2014), the limited number of beach field data including geotechnical properties still hampers the implementation of such properties into beach erosion prediction frameworks (Stark 2016). Therefore, more data, and particularly, field measurements are required to achieve a full understanding of the interaction of beach soil

mechanics and erosion, and to confidently include geotechnical parameters in beach erosion prediction framework.

Shear stresses exerted by fluid flow on beach surface sediments have been measured and documented by numerous researchers in different locations and under different conditions and can be estimated using resulting relationships (Hsu 1972; Nielsen 1992, 2002; Barnes et al., 2009; Puleo et al., 2012). However, measurements of the sediment strength and the friction angle of beach sediments are still rare and are in the majority of cases related to a detailed geotechnical characterization of the sand instead of being part of a beach site investigation (e.g., Gori and Mari 2001; Lade and Abelev 2003; Kim and Sture 2004). Most friction angles used to predict sediment transport are approximated as $\varphi = 32$–$33°$ instead of using actual measurements. This ignores potential deviations associated to gradation, particle angularity, or bulk density (Kirchner et al., 1990; Stark et al., 2014). As the friction angle φ is

directly related to the soil's shear strength τ_f through

$$\tau_f = \sigma \tan \varphi \qquad (1)$$

with σ being the normal stress on the plane of failure, and for the case of cohesionless sediments such as many beach sands (Briaud 2013). Some additional considerations are of importance when discussing friction angles of surficial beach sediments. The friction angle of loose, dry sands under negligible normal stresses can be assumed to approach the angle of repose (Briaud 2013). Different states of sediment saturation will alter the soil's shear strength. Under full saturation, the normal stress is decreased to the effective normal stress and the friction angle represents the effective stress friction angle. Furthermore, undrained conditions may apply under rapid loading where loads are not only transferred to the soil skeleton, but also to the pore water. Under conditions of partial saturation, water surface tension between the sand particles can create an apparent cohesion that adds to the frictional shear strength (Kim and Sture 2004; Briaud 2013). Special attention should also be given to the measurement of friction angle and shear strength, as many traditional geotechnical methods utilize significant normal stresses to simulate soils at deeper sediment depth. Friction angles under low normal stresses tend to be higher. Stark et al. (2017) documented that direct shear tests performed at normal stresses of 24, 48, and 72 kPa (after ASTM D3080) yielded approximately 90% of the in-situ loose surface friction angle of beach sand derived from tilt table tests.

Pore water pressure response has been proven to potentially impact sediment beach erosion in different ways. Residual sediment liquefaction at beaches can be achieved through pore pressure built-up in response to earthquake shaking or ocean storm waves (Kishida 1970; Obermeier et al., 1989; Al-Tarazi 2000; Sumer 2014). Turner and Nielsen (1997) showed that vertical pressure gradients can lead to upward directed pore water flow, and resulting sediment fluidization, or momentary liquefaction. Sleath (1999) and later Foster et al. (2006) demonstrated that horizontal pressure gradients in oscillatory flows can lead to plug formation, and incipient motion. Furthermore, it may be hypothesized that not only full sediment liquefaction impacts sediment erosion, but that even short-termed elevated pore pressure gradients or flows may contribute to a decrease of the threshold shear stress to initiate moti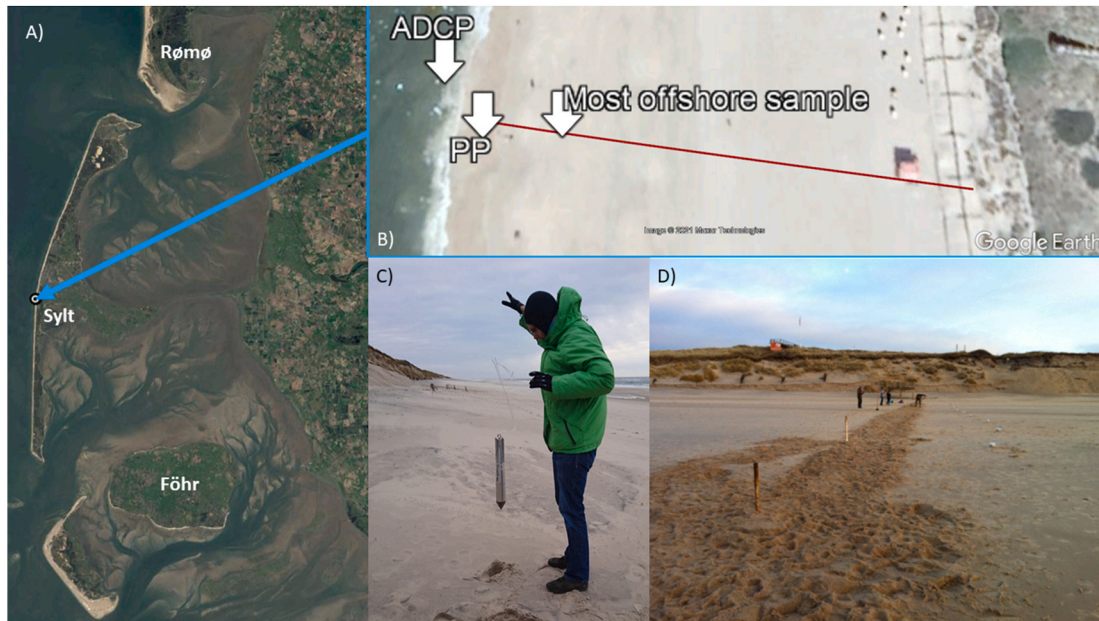on (Tonkin et al., 2003). While some authors have proposed a modified estimate of critical shear stress or of the Shields parameter (e. g., Yeh and Mason 2014), or even a new incipient motion parameter based on pore pressure impacts, there is still a severe lack of field data that prohibits the development and general validation of an updated framework (Turner and Masselink 1998; Butt et al., 2001; Sleath 1999; Foster et al., 2006).

The research objectives for this study were to (i) measure sediment strength and geotechnical properties of beach sand along a cross-shore transect, and (ii) measure the pore pressure response to wave forcing at surficial sediment depths (≤ 0.5 m) relevant for potential liquefaction at a sandy beach at the west coast of the island of Sylt, Germany. Furthermore, (iii) the potential role of the pore pressure behavior on geotechnical properties and on local sediment remobilization processes was explored. The results represent a short field data set with a focus on geotechnical parameters and vertical pore pressures, and further analysis of the pore pressure data using a one-dimensional-vertical (1DV) model.

2. Regional context

The island of Sylt is the northernmost German barrier island in the North Sea (Fig. 1A). It has a length of about 38 km, a width of about 13 km, and is located 9–16 km from the mainland coast. Sylt's western beaches have been subject to numerous research studies related to coastal erosion, morphodynamics, as well as beach nourishment (e.g., Hanson et al., 2002; Richter et al., 2003; Pleskachevsky et al., 2009). Sediments along Sylt's coast consist of reworked moraine deposits and Holocene sands with sand dominating the survey area (Anwar 1974; Lindhorst et al., 2008). Annual erosion rates in excess of 1.4 m were recorded in some locations between 1951 and 1984 (Fachplan Kues-tenschutz 2015; Bundesamt fuer Umwelt 1998). Beach nourishment has been carried out since the 1970s (Liebermann 2007). Beaches around Westerland (just north of the measurement site) have been subject to sediment volume changes in excess of $2*10^6$ m^3 associated to storm events (Fuhrboter 1991; Verhagen 1993). Beach tourism is highly important for the island's economy, making beach conservation a priority.

Field measurements were carried out from January 7th - 10th, 2017,

Fig. 1. A) Google Earth image showing the island of Sylt (Google Earth 2015). B) Google Earth image showing the location of the acoustic Doppler current profiler (ADCP), the pore pressure sensors (PP), and of the portable free fall penetrometer (PFFP) and photo stereogrammetry transect (PSG). The latter transect included 20 measurement position. C) PFFP deployment in the intertidal zone. D) Pipes representing the anchoring for the PP.
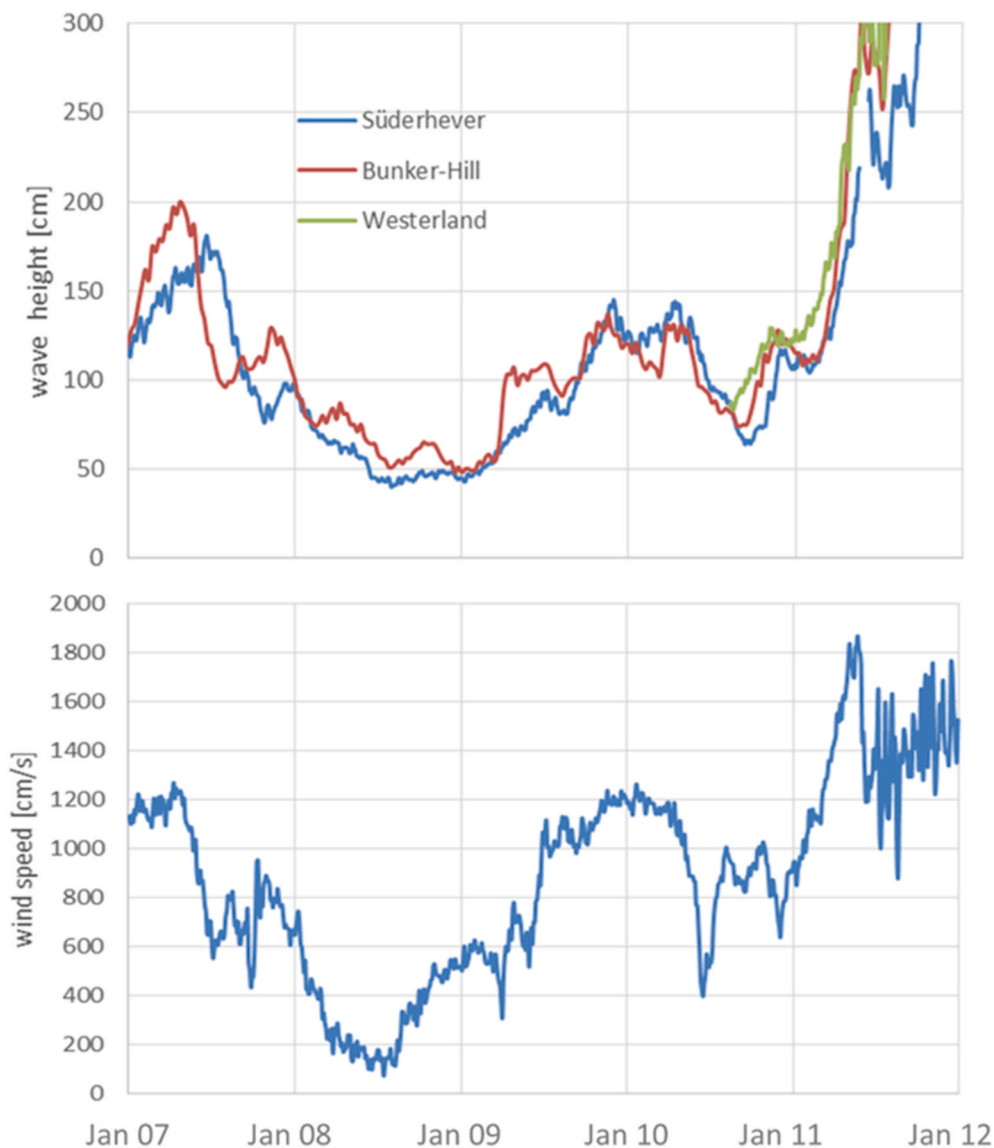
at the western beach south of Westerland (Fig. 1A). During this period, tidal water levels were predicted as low as 4.08 m and as high as 5.95 m relative to zero of the Westerland gage 110039 which is −5.01 m of DHHN2016. Fig. 1A depicts water levels approximately at a similar level as low water conditions during the survey period with the acoustic Doppler current profiler (ADCP) being deployed in the upper subtidal zone, the pore pressure sensor stack in the lower intertidal zone (PP in Fig. 1B), and portable free fall penetrometer and sediment sampling being performed along a cross-shore transect (red line in Fig. 1B) with sediment sampling not covering the full transect (see "most offshore sample" mark in Fig. 1B) due to rising waters. Based on the predicted water levels, a typical average beach slope of ~1.3% in the area of interest (Otto et al., 2021), and observations during the survey period, high water levels reached up to approximately the most onshore test locations just underneath a beach scarp at the toe of the dunes (Fig. 1D). Local wave statistics from 2016 documented a maximum offshore significant wave height of $H_s = 5.51$ m measured in December less than a month prior to the field survey (BSH 2017). The nearshore wave height is affected during high energetic events by a breaker bar with a varying depth of about 2.5–4 m. Most energetic waves approached from the North-West (BSH 2017). Wind speed and wave measurements are shown

in Fig. 2. The station Westerland was located 4 km away from the measuring location. Additional wave measurements from buoys several kilometers away (namely, Süderhever and Bunker-Hill) fill a gap in the wave buoy record from Westerland and serve the purpose of providing a measure of wave conditions during the measurements (Fig. 2).

Beach topography or nearshore bathymetry were not measured and are unfortunately unavailable from other sources during this survey period. As the beach is undergoing significant erosion events and beach nourishments, historic beach profiles were not compared in detail to the measurements conducted in this survey. However, the intertidal zone is typically relatively flat with an average beach slope of approximately 1.3% (Otto et al., 2021, also see Fig. 1D). More recent sediment deposits were apparent in front of the dune toe (Fig. 1C), representing an area were dune fencing has been applied to enhance sediment accumulation (Fig. 1B and C). It may be speculated that those deposits stem from dune front slope failures and the visible scarp (Fig. 1C and D).

3. Methods

Field measurements were limited to a cross-shore transect stretching from the upper subtidal zone across the entire intertidal zone to dune

Fig. 2. Significant wave height (upper panel) and wind speed offshore of Westerland (lower panel) in January 2017 during the measuring campaign in the proximity of the study site. Data were obtained from BSH.de.

line (Fig. 1B). Measurements included (i) portable free fall penetrometer (PFFP) deployments at 20 locations with three deployments per location (Fig. 1B red line), (ii) continuous pore pressure (PP; Fig. 1B) measurements over a period of 28 h at four sediment depths in the upper 55 cm of the beach face, (iv) sediment grab sampling at the PFFP deployment locations until water levels got too high during the sampling time (Fig. 1B "most offshore sample") and deeper grab samples at PP obtained during installation of the pressure transducers, and (v) acoustic Doppler current measurements (ADCP). The methods of data collection and analysis are outlined in the following.

The field campaign was designed to conduct PFFP deployments and obtain surficial sediment samples well distributed across the intertidal zone. PFFP deployments were conducted as planned, but co-located sediment sampling was limited to locations onshore of the lower intertidal zone due to increased water levels at the time of surveying. Pressure transducers were deployed as planned at the low end of the intertidal zone, where burial was still possible without diver support. Sediment samples were obtained at the same location during installation of the pressure transducers. The ADCP was deployed in the upper subtidal zone, but experienced anchoring issues which led to ambiguous results. Initially planned nearshore PFFP deployments and sediment sampling was prohibited by weather conditions during the survey window. The field campaign was planned as an exploratory study with focus on geotechnical measurements (including pore pressure monitoring) of surface sediments in the intertidal zone which have rarely been conducted in similar settings or with a similar suite of instruments. The lack of larger supporting infrastructure for this exploratory study limited duration and spatial extent of this study.

The portable free fall penetrometer *BlueDrop* was used with a conical tip geometry (Fig. 1C). The probe has a mass of about ~8 kg, and a length of ~63 cm. It measures acceleration with an accuracy of better than 0.1 g (g being gravitational acceleration) and up to 250 g, and hydrostatic pressure up to about 2 MPa at a sampling rate of 2 kHz. More details on the instrument, typical deployment strategies, and the type of data measured and derived can be found in Stark and Ziotopoulou (2017) and others. The device is commonly used for the rapid geotechnical investigation of subaqueous seafloor sediments. In this study, it was deployed along a subtidal to subaerial beach transect (Fig. 1C). Similar to subaqueous environments, the motivation to deploy the PFFP was to rapidly assess in-situ strength of the beach surface sediments. An advantage of the PFFP over other methods is that it can easily be deployed in the swash and subtidal zone, and no change in instrumentation is needed when transitioning from emerged to submerged conditions. Deployment strategy and data processing were carried out similarly to in-water deployments, using the probe's deceleration during impact and soil penetration to determine sediment resistance force via Newton's second law. Special care was given to having the penetrometer hanging straight and motionless prior to release. It was released from a height of about 80 cm above the beach face. Sediment strength is expressed as the so-called quasi-static bearing capacity (QSBC) that considers the maximum sediment resistance force at different sediment depths, the loading surface area of the probe, and an estimated strain rate correction (Stark and Ziotopoulou 2017). Strain rate effects result from a dependence of the soil's shear strength to strain rate with often higher sediment strength being experienced for faster penetration or shearing processes (for a detailed discussion on the relevance for free fall penetrometers, please see, e.g., Steiner et al., 2014). The strain rate correction applied in this study has previously been applied to sandy seabeds (e.g., Stark et al., 2009, 2012; Albatal et al., 2019). However, there are some limitations associated to this method, and particularly to the strain rate correction that are still subject to research (see Discussion). The approach is based on the assumption that the deceleration of the probe upon impact and during penetration is solely due to the sediment resistance, and that other factors such as drag forces are negligible. Particularly for the case of deployments in air and penetration into sand, this assumption is

acceptable.

Sediment grab samples were extracted using a trowel at most of the PFFP locations. No samples were successfully extracted at most seaward deployment positions, due to the water depth and wave action at the time of sample collection. At most sample locations, the upper 10 cm of the beach surface were collected. Parallel to the pore pressure sensors (i. e., at the same cross-shore distance), sediment samples were collected in 10 cm thick increments up to a sediment depth of 40 cm. Standard direct shear testing of sediment samples was carried out in the geotechnical laboratories at the Technical University of Darmstadt following DIN 18,137. Shear tests were performed at normal stresses of 10 kPa, 15 kPa and 20 kPa, with a displacement velocity of ~0.04 mm/min, and at initial sediment densities ranging from 1.5 to 1.6 g/cm³. The tests were performed on saturated samples. Additionally, sand samples were sieved to measure the grain size distribution. From the grain size distributions, upper and lower bound permeability and void ratios were estimated for sediment samples extracted at the location of the pore pressure transducers (*PP* in Fig. 1B), and the hydraulic conductivity k_f was approximated using Taylor (1948) based on Hazen (1911):

$$k_f = 100D_{10}^2 \tag{2}$$

with D_{10} being the effective grain size (i.e., 10% by weight of the sample are smaller and 90% by weight are larger than D_{10}).

Pore pressure data was collected from January 8, 2017, 12:00 h local time to January 9, 2017, 16:00 h local time, measuring from daylight low tide throughout two high tides to the next daylight low tide using *RBR SoloD*s pressure sensors operating at 10 Hz. Four pressure transducers were arranged in a vertical array at location *PP* as indicated in Fig. 1 B). For the deployment, a vertical steel pipe was driven into the sand, and a minimum amount of sediment was excavated using small hand shovels that enabled the placement of the approximately 15 cm long and 2.5 cm thick pressure transducers along the steel pipe (Fig. 1 D). Finally, sediment was infilled, and compacted by tapping by hand to a density that appeared similar to the natural surroundings. Nevertheless, it is expected that the sediment packing was disturbed from burial, and therefore, the first high tide of measurements will be ignored. It is assumed that local sediment transport, swash and waves re-compacted the surficial sediment to its natural state during the uprising flood and retreating ebb tide. If this assumption would be challenged, the bulk densities would likely be smaller than the undisturbed in-situ conditions. Initial sensor burial depths equaled ~10 cm, 25 cm, 40 cm, and 55 cm, respectively.

Wave conditions were investigated with regards to four measurement periods of 15 min each during the passing swash zone during flood tide, fully submerged flood tide, high tide, and ebb tide. Statistic wave characteristics (significant wave height, peak period, maximum wave height, and mean wave height) were compared for the different burial depths within each investigated time period. Additionally, the phase lag in degrees with respect to the top sensor (at ~10 cm of sediment depth) was determined. Drainage conditions were also evaluated at low tide between the two measured high tides.

Acoustic Doppler current profiler (ADCP) data were collected but yielded unclear results due to movement of the anchoring platform and limited water depth. The data have been excluded from further analysis. Photogrammetric analysis of the PFFP deployment areas were out of the scope of this manuscript.

4. Results and discussion

In the following sections, results obtained from laboratory testing of sediment samples, from PFFP deployments along a cross-shore transect (Fig. 1), and from vertically stacked pore pressure sensors in the lower intertidal zone embedded in the upper meter of the beach sand are shown. Cross-shore variations of geotechnical and sedimentological properties are discussed with regards to exposure to marine and aeolian

processes. Pore pressure observations are discussed with regards to the local sediment properties, tidal and wave influences. Finally, an initial numerical simulation is used to relate pore pressure measurements to existing numerical expressions. The data set serves the purpose to contribute to our understanding of the relations between geotechnical sediment properties, soil-pore water processes, and beach dynamics (e. g., Nielsen et al., 2002; Mory et al., 2007).

4.1. Sediment samples

Sediment samples along the cross-shore profile featured median grain sizes of $d_{50} = 300$–850 μm (Fig. 3) with the finest sediment near the dune toe and fenced areas (Fig. 1B and C), coarser sediments in the central intertidal zone, and the coarsest sediments in the lower intertidal zone (Fig. 3). No sediments were collected in the subtidal zone. The coarsest sediments (>600 μm) were observed in the lower intertidal zone. The surface sediment sample close to PP was characterized by d_{50} = 516 μm (coarse sand after Wentworth 1922) and was moderately sorted (0.86) after Folk and Ward (1957). At the same location and sediment depths of 20–40 cm, sediments were very coarse sand with d_{50} = 1037–1365 μm (Table 1) and poorly sorted (1.01–1.49). Sediment fining at the upper beach and towards the dune toe can be associated with governing aeolian sediment transport that also likely led to the deposition of sediments in the areas featuring dune fencing at the toe of the dune. Coarser sediments in the central and lower intertidal zone are likely associated with governing marine processes and particularly the exposure to the shore break. Very coarse sediment layers may relate to previous storm events when energetic hydrodynamic conditions removed finer sediments. Such observations are in line with, e.g., van der Wal (2000) who documented differences in the abundance of finer sediments between zones dominated by aeolian processes versus marine processes at a nourished beach on Ameland, the Netherlands. Similarly, Gallagher et al. (2016) argued that the presence of coarse sediment deposits in Duck, NC are related to the reworking of sediments by the shore break.

Friction angles determined from direct shear tests followed a similar cross-shore trend. The smallest friction angles (φ = 34–41°) were measured for sediment samples from the subaerial zone. Friction angles ranging from φ = 36°–42° were determined for sediment samples from the upper intertidal zone, and friction angles from φ = 38°–44° were measured in the lower intertidal zone. Thus, friction angles exhibited a slight increasing trend seaward. Overall, it can be noted that the friction angles are higher than values often applied for sediment transport considerations (~32–33°).

Estimates of void ratios (i.e., ratio of volume of voids to volume of solids in a soil) were determined from the grain size distributions and ranged from $e_{min} = 0.5$ to $e_{max} = 1$. Thus, porosities can be assumed to range from 33% to 50%. These values seem in line with values reported in the literature for clean (little to no fine content) coarse sands with void ratios ranging for example from 0.538 to 0.767 for a Cambria sand with a $d_{50} = 1500$ μm and from 0.6 to 0.98 for a Host sand A2 with 250 μm (Cubrinovski and Ishihara 2002). Atkins and McBride (1992) reported porosities of beach sands from 39 to 49%. Following Taylor (1948), the hydraulic conductivities of sediment samples in the upper 40 cm of the beach surface ranged from 0.06 cm/s at the surface to 0.11–0.15 cm/s at 10–40 cm of sediment depth (Table 1). For comparison, estimates after the U.S. Bureau of Reclamation (USBR)/Bialas and Kleczkowski (1970) and after Beyer (1964) are provided in Table 1 as well. These values fit well into the suggested range for clean sands by Terzaghi and Peck (1948).

4.2. Penetrometer results

The time of the penetrometer measurements coincided with an early

Table 1
Estimated values of hydraulic conductivity k after Taylor (1948)/Hazen (1911), USBR/Bialas and Klecxkowski (1970), and Beyer (1964).
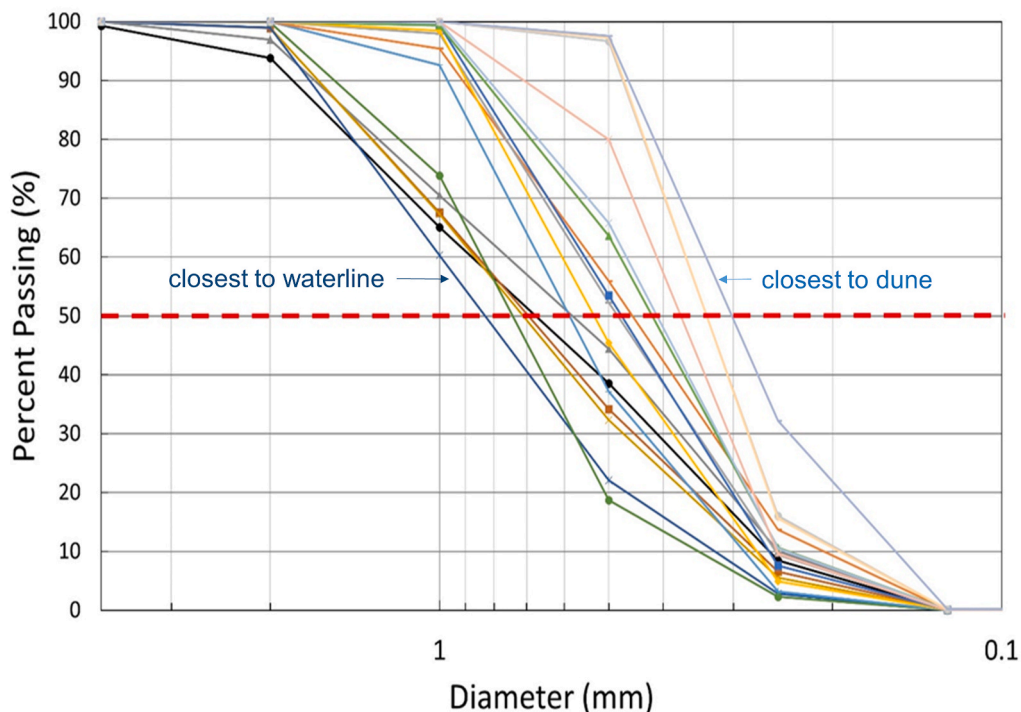
Sediment depth (cm)	d50 (μm)	kf Taylor (cm/s)	kf USBR/Bialas (cm/s)	kf Beyer (cm/s)
0–10	580	0.06	0.026	0.054
20/Oct	1365	0.15	0.11	0.12
20–30	1037	0.11	0.062	0.1
30–40	1090	0.13	0.078	0.11

Fig. 3. Grain size distributions of cross-shore samples representing the upper 10 cm of the beach face with sediment coarsening from the dune toe to the waterline.

flood tide, i.e., PP was located in the swash zone. Three independent penetrometer drops were carried out at each location, with a distance of ~1 m from each other to avoid effects from previous deployments on the measurement. Fig. 4 shows the recorded deceleration profiles over the penetration depth of three drops carried out in the subaerial zone. The three deployments are consistent with penetration depths limited to 11–13 cm and a maximum deceleration of 14.0–14.5 *g*. In all cases, the deceleration increased rapidly after an initial penetration of 2–3 cm where the penetrometer experienced ~0.5 *g* of deceleration (Fig. 4). Impact velocities for these deployments ranged from 3.9 to 4.2 m/s (Fig. 5). Impact velocities throughout all 60 drops along the entire transect were, on average, 3.7 m/s with a standard deviation of 0.28 m/ s, highlighting consistency in the deployment method. Fig. 5 shows the estimated QSBC profile determined for drop 1 shown in Fig. 4. It shows a rapid increase in sediment strength achieving a maximum of ~25 kPa, being representative of the penetrated top 10 cm of the beach surface. In comparison to available data from the literature collected in areas of submerged sandy seabed sediments (e.g., Stark et al., 2012), the QSBC values shown here were overall significantly smaller, i.e., the beach sand was less resistant against the PFFP.

Fig. 6 shows the penetration depth, maximum deceleration, and maximum estimated QSBC along the cross-shore profile. Highest penetration depths and weakest sediments were found in the (yellow) subaerial zone. Sediment strength increased with some fluctuations within the intertidal (cyan) zone. The reason for relatively strong sediments at a distance to the waterline of ~35 m is not known and would be speculative. Sediment strength exhibited a strong increasing trend while penetration depth decreased in the swash (blue) zone. The highest sediment resistance, with QSBC >100 kPa, was measured at the most offshore measurement location, representing a mean water depth of about 60 cm at the time of deployment. Such values are in line with measurements of submerged nearshore sands, measured by the same device (Albatal and Stark 2016; Albatal et al., 2019). Following a novel approach proposed by Albatal et al. (2020) for the same probe, the penetrometer results would suggest in-situ friction angles ranging from 38 to 45° in the submerged areas tested and in the swash zone. This is well in line with the results from direct shear testing of samples from the lower intertidal zone. The significant increase in sediment resistance in the surf and swash zone are likely related to a combination of sand densification from wave action (Dean and Dalrymple 2004) as well as strained rate effects and rapid undrained loading (White et al., 2018;
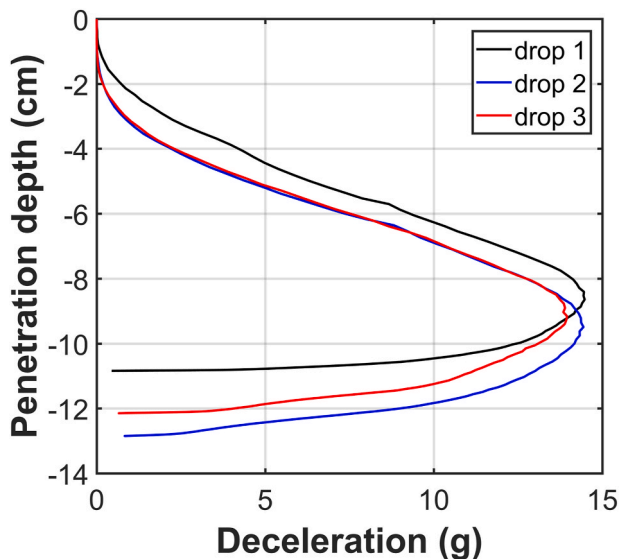

Fig. 5. Deceleration (blue line), impact and penetration velocity (dashed line), and estimated quasi-static bearing capacity (black line with uncertainty indicated in grey) for drop 1. The depicted decrease of QSBC towards the end of penetration represents an artifact of the data processing method. (For interpretation of the references to colour in this figure legend, the reader is referred to the Web version of this article.)

Albatal et al., 2020). As the method by Albatal et al. (2020) addresses strain rate effects, it is assumed that this increase in sediment resistance is mostly related to densification of sand from wave action, but this remains unproven due to a lack of undisturbed samples here.

4.3. Pore pressure – on tidal scale (5 min averages)

Pressure transducers p_1 to p_4 were deployed on January 8, 2017, at 12:00 local time and were switched off on January 9, 2017, at 16:00 local time after recovery. Accounting for potential disturbances due to initial sensor burial, data analysis did not start until more than 8 h after deployment of the sensors. Thus, measurements of the first flood and high tide were omitted from analysis. The measured pressure in the period of data analysis is displayed in the upper panel of Fig. 7. The high tide just preceding the period of data analysis as shown in Figure occurred at 20:47 local time with a predicted high water of 5.76 m according to the Westerland waterlevel gage (110039). The following low tide was predicted at 03:28 local time with a water level of 4.19 m. The shown high tide occurred at 9:22 local time with a predicted water level of 5.92 m, followed by low water at 16:13 local time and a water level of 4:09 m. The lower panel of Fig. 7 shows 5 min averages of the recorded data set, reflecting those tidal periods. Two ebb tides (0–300 min; 750–1050 min), a low tide phase when the mean surface water level was below the sensor location (in the cross-shore direction) (300–500 min), and a flood tide (500–750 min) are shown. For most of the phases, the four sensors exhibited similar behavior throughout the time record. Differences in pressure between the sensors matched well with the targeted vertical distances of 10 cm. Effectively, the distance between sensors p_1 - p_2 and p_3 - p_4 appeared slightly wider (~12–13 cm), and between sensors p_2 - p_3 slightly closer (~9 cm). This was likely associated to not perfectly horizontal sensors (being slightly tilted upwards/downwards). Pressure sensor p_1 was located ~11 cm from the beach surface at the time of deployment. A maximum mean high water (i.e., above beach surface) of about 80 cm was measured during high tide, being in line with expectations.

Two additional observations can be made: First, the two recorded ebb tides differed somewhat. While the first was characterized by an approximately steady decrease in hydrostatic pressure, and therefore, water level, the second ebb tide exhibited a more rapid water retreat followed by a break in this trend and following slower decrease of water levels. Second, the decrease of groundwater levels was steady and

Fig. 4. Deceleration recordings vs. penetration depth measured by the portable free fall penetrometer at one cross-shore location in the subaerial zone. Each drop is an independent deployment approximately 1 m away from each other.
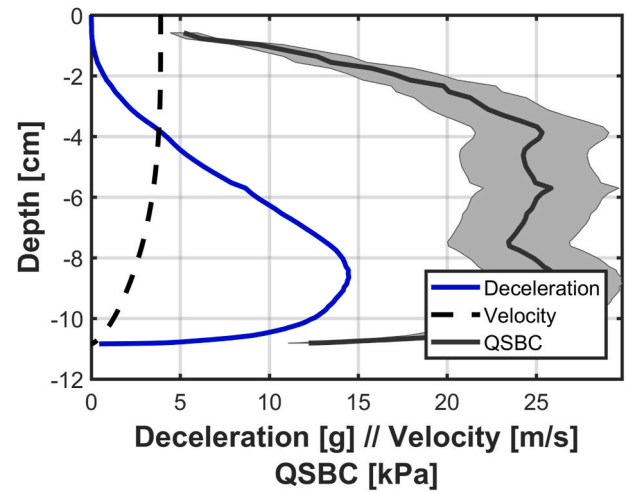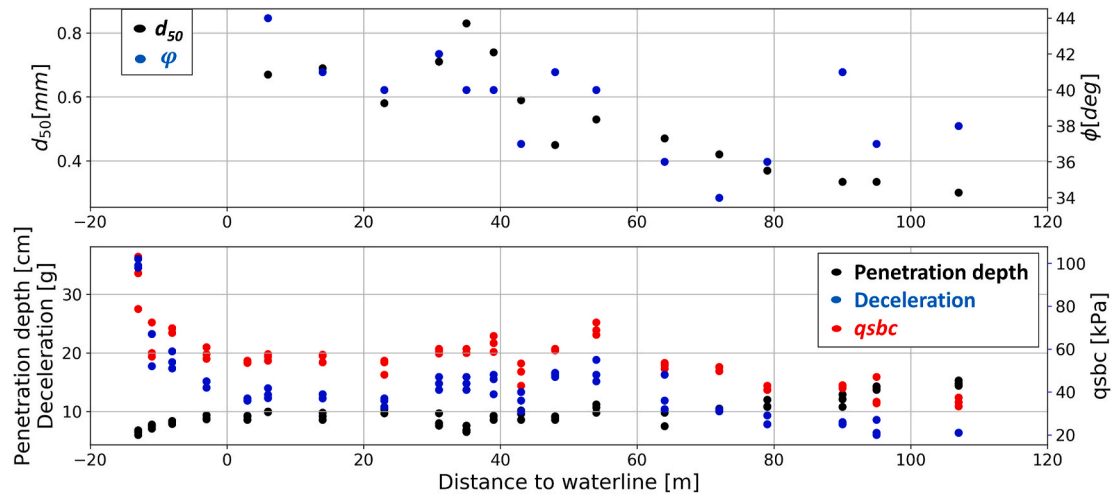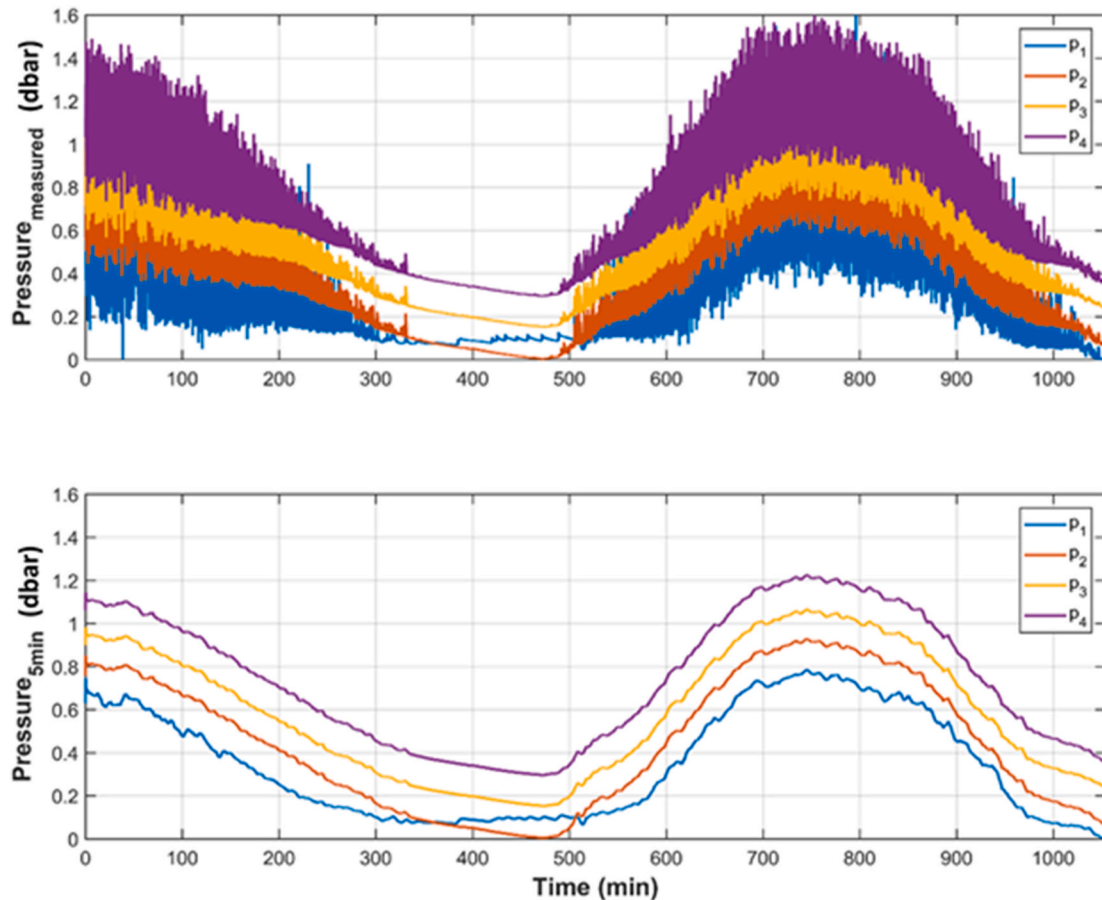
Fig. 6. The median grain size (d_{50}) and the friction angle obtained from laboratory testing of surficial sediment samples are displayed in black and blue, respectively, in the upper panel. In the lower panel, the penetration depth (black), maximum deceleration (blue), and estimated maximum quasi-static bearing capacity (*QSBC*; red) as obtained by the PFFP are shown. The cross-shore transect is displayed relative to the location of the waterline during PFFP testing and sediment sampling and with 0 m indicating the waterline. It should be noted that sediment sampling was not carried out in submerged locations (distance to waterline <0 m). (For interpretation of the references to colour in this figure legend, the reader is referred to the Web version of this article.)

Fig. 7. Hydrostatic pressure measurements (upper panel) versus time (minutes), and 5 min averages versus time (lower panel). The displayed time of analysis excludes the initial low to high tide due to likely initial sediment disturbance by the burial process.

consistent for sensors p_2 - p_4. However, the sensor closest to the surface p_1, seemed to maintain water levels of ~10 cm. The groundwater drainage and recordings of p_1 will be discussed in more detail in the following section.

4.4. Pore pressure – low tide and drainage

Data was recorded over one entire low tide. Fig. 8 displays 200 min of recorded pressures covering the low tide (predicted on January 9 at 3:30 local time). Focusing on the deeper pore pressure transducers first
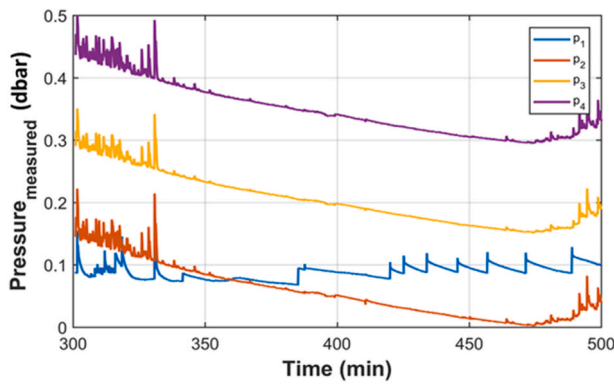
Fig. 8. Hydrostatic pressure measurements versus time (minutes) of drainage phase.

(p_{2-4}), it is evident that all sensors suggest a similar loss of pressure head. In fact, over the measurement period of 340–460 min, the decrease in water depth with time can be approximated as being linear with a drainage rate of ~0.013 cm/s. This is about ten times larger than the estimated hydraulic conductivity at these sediment depths (vertical direction) (Table 1). However, it should be considered that no vertical drainage is expected, but rather drainage directed seaward and through the beach face is expected (Turner 1993; Masselink et al., 2014). Allowing a beach slope estimate of 5.7° after Dette and Raudkivi (1994), then the monitored drainage rate would indeed match the estimated hydraulic conductivity (0.06 cm/s at the surface and 0.11–0.15 cm/s at 10–40 cm of sediment depth) assuming approximately horizontal and seaward directed drainage as suggested by Turner (1993). Drainage rates appeared consistent between sensors p_{2-4}, which is also in line with the limited variations in estimated hydraulic conductivities and permeability for sediments at vertical depths ranging from 10 to 40 cm (Table 1).
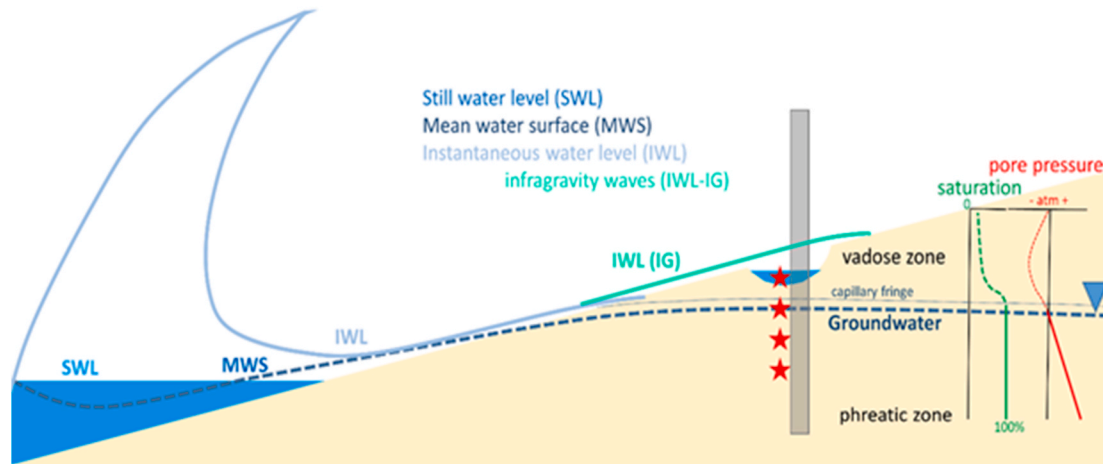
Sensors p_{2-4} clearly display waves until sensor p_2 recorded a pressure of ~0.11–0.12 dbar (i.e., a water head of ~11–12 cm). The wave signatures are consistent between the three sensors. It appears that sensors p_{2-4} were not significantly affected by surface waters when the water head sank below 11 cm above sensor p_2, i.e., the surface water line moved seaward of the sensor location PP, and water heads were associated with ground water. This also represented a first indication of surficial sediment erosion at PP that likely reduced the burial depth of all sensors by ~11 cm, leading to exposure of p_1. Furthermore, it can be noted that groundwater levels were lowered to the burial depth of sensor p_2, indicated by the hydrostatic pressure approaching zero dbar (please note that the record was corrected for atmospheric pressure). p_3 and p_4 were located below the groundwater level at all times of the recording.

The data recording by p_1 however raises some questions and complexity. The data recorded by p_2 to p_4 suggest that towards the low tide sediment was drained to a sediment depth of almost 25 cm (location of p_2), while the topmost sensor p_1 at an initial sediment depth of 10 cm appeared to have experienced a continuous water head of approximately 7–8 cm with occasional swash run up reaching the sensor. Similar shapes of rapid infiltration and slow diffusion of the water pore pressure head have been documented by Turner (1998) in the swash. However, the time of pore pressure diffusion was on a time scale of 5 min with an initial maximum vertical flow from the pressure gradient of ~0.06 cm/s, and the surface appeared to experience full drainage. In our case the surface seems to just fully drain approaching a water head of <9 cm at a similar sediment depth of the sensor. The approach and infiltration of the water front appeared always relatively instantaneous (with a water head of ~3 cm), and an initial rapid drainage followed (water head of ~1 cm). However, pore pressure diffusion or drainage seemed to slow down significantly then with periods in excess of 10 min, leading to vertical flow from pressure gradients of approximately 0.003 cm/s,

representing 5% of the hydraulic conductivity previously estimated for the surficial beach sediments. It should also be mentioned that these run up events are not displayed by sensors p_2 to p_4 which is not in line with observations by Turner (1998) to a sediment depth of 34 cm.

An obvious explanation of this observation seems that there is a bias in the recording of the top sensor. However, all sensors have been tested and validated before and after the experiment and did not show any signs of instrument failures. This is also confirmed by the fact that the sensor falls well in line with the other sensors and expectations during flood, high and ebb tide (Fig. 7). Mechanical pressure bias on the transducer face by sediment particles was mitigated by using a coarse porous plastic shield and a geotextile and was confirmed by observations of no contamination after the experiment. The beach face can be considered dynamic. Therefore, additional burial or exposure of the top sensor was likely. Indeed, p_1 was found exposed and slightly tilted upward during a quick check up at the low tide at night, as well as at the time of recovery. A scour hole had formed around the anchoring pipe. The anchoring pipe had an outer diameter of about 10 cm. Therefore, the development of a scour hole with depths just in excess of 10 cm is feasible (Sumer et al., 1992). Likely, this resulted in an initial exposure of the top sensor, leading to subsequent upward tilting of the sensor as well as scour hole widening, and potentially deepening. It was also observed that the scour hole mostly sustained a small puddle of water that was furthermore fed by infragravity waves reaching up the shore. Infragravity wave run up with periods in excess of 5 min has been observed in numerous locations (e.g., Holman et al., 1978; Schaeffer 1993; Sheremet et al., 2002) and has also been observed in this area (Houser and Greenwood 2007). In fact, Montano Munoz (2015) stated that swash hydrodynamics are dominated by infragravity energy at the beaches of Sylt during storm events. Initial diffusion of the upper 1 cm of the pressure head introduced by the run up is rapid. However, the subsequent drainage rate is low, being in line with a smaller hydraulic conductivity of surface sediments (Table 1), and the observed formation of sustained puddles.

Interestingly, the observations at p_1 and at p_{2-4} appear to be entirely decoupled as soon as location PP slipped into the upper swash zone, and even more so when only infragravity waves reached the location. The authors are not aware of any documentation of such a decoupling between surface waters and groundwaters at sediment depths in excess of 10 cm. Slightly finer sediments with a lower hydraulic conductivity seem to be an insufficient explanation, considering the estimated hydraulic conductivity. At this time, the groundwater exit point (if present) can be assumed to located seaward of PP. A vadose zone with capillary fringe, i.e., negative pore pressures and a mixture of air, water and sand has likely developed above the location of p_2, representing a sediment depth of ≲12 cm (Fig. 9). Negative pore pressures and partial saturation may decrease hydraulic conductivity in comparison to the expected values in line with the sediment type and grain size (Van Genuchten 1980; Tuller and Or 2001). Furthermore, air enclosures would dampen hydrostatic pressure signals from above the vadose zone and for the sensors in the phreatic zone. This means that some amount of the infragravity wave run up would be directed downslope as backwash hampered from infiltration by a limited hydraulic conductivity. Second, the lowered hydraulic conductivity contributes to slow drainage as observed at p_1, while air enclosures dampen these surface signals, leaving them unnoticed by p_{2-4}. Such a conclusion would suggest that the formation of a vadose zone may have a larger impact on swash behavior, groundwater processes, and associated sediment transport than currently considered by forming a stiff layer of reduced infiltration or exfiltration. However, it should also he highlighted that our observations were limited to one full low tide at one location of the beach, and that further investigations of this issue are needed to confirm or reject this hypothesis. Further investigations should include a longer time series, measurements at different cross-shore and possibly long-shore locations, as well as at different sites with different geomorphology and hydrodynamic conditions. Such more focused investigations should also

Fig. 9. Conceptual sketch of low tide situation. Not to scale; based on concepts presented by Horn (2002, 2006). Red stars are indicating the locations of the pressure sensors, the grey box represents the anchoring pipe. (For interpretation of the references to colour in this figure legend, the reader is referred to the Web version of this article.)
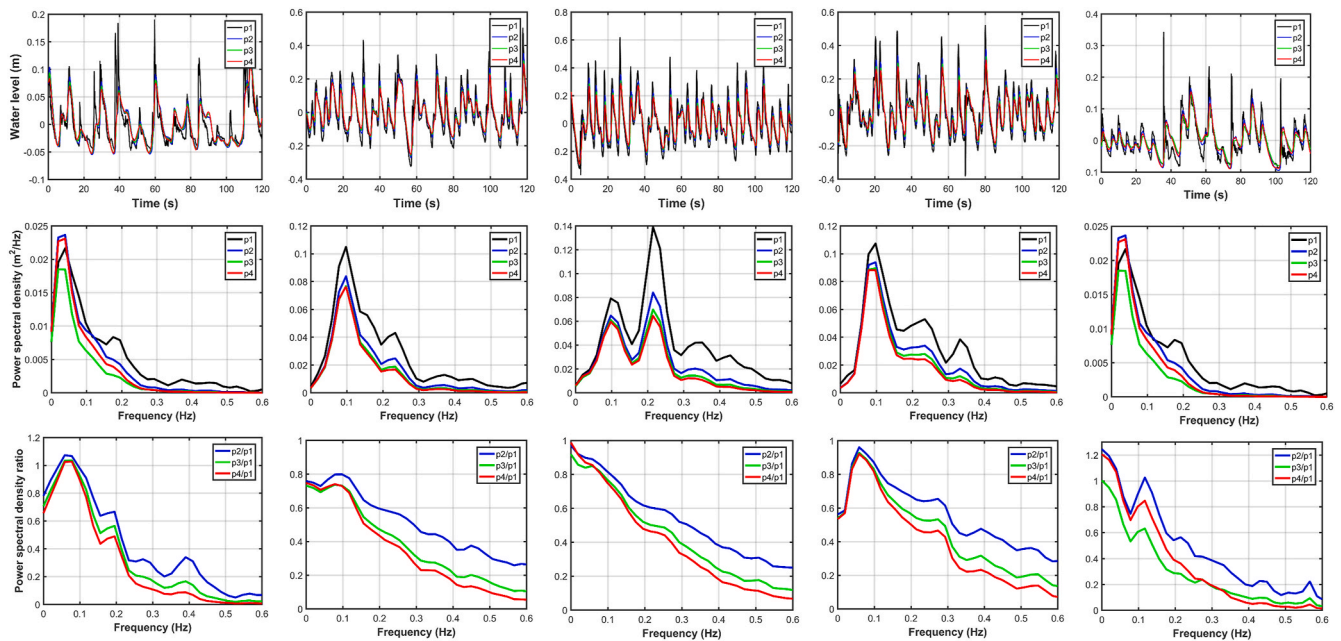
consider higher vertical resolution through more sensors.

Fig. 9 depicts the processes described above. Similarly as described by Horn (2002, 2006) and others, sediment saturation is assumed to be 100% below the groundwater table and approaching 100% in the capillary fringe (if present). The exact profile of the state of saturation with depth depends on sediment properties, but also on environmental factors like air temperature, solar radiation, etc. Associated with such variations in the actual saturation profile, variations in the vertical profile of pore pressure (in excess of atmospheric pressure) are expected. On a tidal time scale, pore pressure below the groundwater table reflect hydrostatic pressure. Horn (2002, 2006) suggested an approximately exponential increase of negative pore pressure (with 0 being atmospheric pressure). Starting from the groundwater table, this is a feasible model. However, depending on the distance to the surface and considering water-retention curve behavior, a decrease of negative pore pressures towards the surface may be considered.

4.5. Pore pressure measurements on wave scale

Two minute long excerpts of the wave recordings (10 Hz) from early flood, late flood, high water, early ebb, and late ebb tide during the second recorded tidal cycle with respective average water levels of 16 cm, 56 cm, 77 cm, 66 cm, and 13 cm were analyzed (Fig. 10). The waves are well reflected by the pressure recordings of all sensors, enabling a correlation of the wave recordings at the different sediment depths. No offsets were identified between the sensors, confirming that the sensors were well stacked within a vertical profile. Based on the discussion of the previous section, p_1 will be considered representative of the wave conditions at the seabed without impacts of sediment embedment for the lack of additional measurements and acknowledging that the measurements may have been affected by some sediment coverage until the scour hole evolved.

Waves were irregular, i.e. the length of individual waves differed and

Fig. 10. Two minutes long wave recordings (upper panels) of all four vertically stacked pressure transducers after detrending (removal of tidal signal) during early flood, later flood, high tide, early ebb, and later ebb of the second recorded tidal cycle. The vertically central panels show the associated power spectra. The lower panels show the power spectral density ratios between p_2/p_1 (blue), p_3/p_1 (green), and p_4/p_1 (red). (For interpretation of the references to colour in this figure legend, the reader is referred to the Web version of this article.)

the shape of the waves was asymmetric and skewed as expected in this shallow water environment. Increased wave damping with sediment depth was observed in the wave signals, the associated power spectra, and the power density spectral ratio between the three buried sensors and the top sensor, respectively. Two observations can be made: First, wave damping eliminated almost all high frequency signals, particularly when they carried little energy (flood and ebb cases when water depths <70 cm). Second, wave damping with sediment depth did not increase linearly, but damping increased noticeably from p_2 to p_3, while the wave signatures and power spectra of p_3 and p_4 seemed almost similar. The latter can also be highlighted by plotting the significant wave heights versus sediment depth (Fig. 11 left panel). During high tide, the significant wave height decreased approximately negative-exponentially with sediment depth. However, this relationship did not apply to the other investigated periods. During early ebb and late flood, slightly less damping was apparent in the uppermost 12 cm, while damping appeared very similar at sediment depths >12 cm. Therefore, it may be proposed that either the sediment surface layer changed in its damping-affecting properties, and/or that the loss of wave energy at the uppermost seabed surface is dependent on the initial wave conditions in the water column and water depth. The peak period (during high tide ~ 4–5 s at the beach surface) remained approximately unchanged with sediment depth. However, it increased slightly by 0.5–1 s with sediment depth. These observations are in line with observations and considerations by other researchers such as Raubenheimer et al. (1998) and Guest and Hay (2017).

The phase lag between the uppermost sensor and the buried sensors was significant with 25–36°, likely due to the tilting upwards position and resulting misalignment of the topmost sensor (Fig. 11 right). Between p_2 and p_3, the phase lag decreased to only 3–6°, and between p_3 and p_4, the phase lag was negligible (0–2°). Therefore, a phase lag can be considered minor to negligible considering potential uncertainties in positioning of the sensors regarding the wave direction. The little observed phase lag however appeared to increase with decreasing water depth, being in line with observations by Guest and Hay (2017) for a mixed sand gravel beach. However, the magnitudes of the phase lag were significantly smaller in this study than in Guest and Hay (2017), likely associated to different saturation behavior of the different sediment types. Raubenheimer et al. (1998) conducted similar measurements at a sandy beach. They concluded that wave attenuation in a sandy shoaling and surf zone was significant particularly with increasing frequencies and shallower water depths. Furthermore, they found that attenuation followed an approximately exponential trend with sediment depth, and that the phase lag was small. These findings match our observations well.
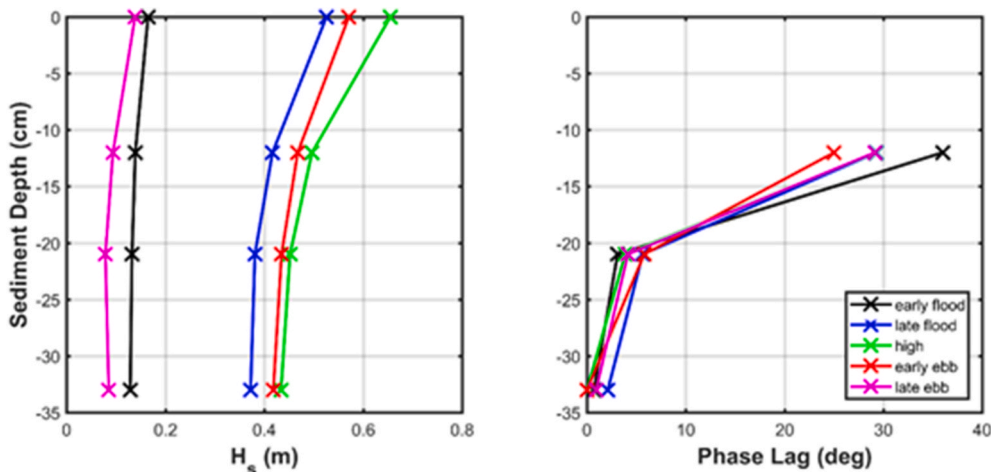
The ratios of power spectral densities of p_{2-4} and p_1 are displayed in the lower panels of Fig. 10 for the investigated periods of the tidal cycle. A ratio <1 would indicate loss of wave energy with sediment depth (i.e., wave damping). This applies to the later flood, high tide, and early ebb, i.e., water depths $\gtrless$ 1 m. A ratio >1 would indicate an overall higher wave energy at higher sediment depth. In the period of early flood, this applies to all three pressure transducers at low frequencies of about 0.08 Hz (12.5 s). During the period of late ebb, this also applies to p_2 and of p_4 sensor at low frequencies <0.02 Hz (50 s), and for the p_2 at ~0.11 Hz (9 s). The available data set is not sufficient to draw detailed conclusions from these observations. However, it suggests rather complex pore pressure conditions with possible favorable conditions for the development of upward directed flows from vertical pore pressure gradients during swash conditions.

4.6. Pore pressure model

The observed pore pressure time series as described in section 4.3 to 4.5 are modeled using a one-dimensional-vertical (1DV) mathematical model. The governing equations of the soil system are given by Biot (1956) and have been applied to the coastal environment by Mei and Foda (1981). These equations have been used by many researchers (Tørum 2007; Qi and Gao 2015). The model accounts for two material phases – the pore fluid and the sediment matrix. Four variables are modeled – the displacement rates of the fluid u and of the sediment matrix v, the pore pressure p and the matrix normal stress σ. The fluid phase represents the pore water including gas. The sediment matrix is modeled as a poroelastic solid with porosity n and Young's modulus E. Both phases are modeled as compressible continua. The bulk modulus of the fluid phase β strongly depends on the gas content. For both phases, momentum and continuity equations result in equations (3)–(6) given below. The phases interact in the momentum equations (4) and (6) strongly due to the friction of the ground water flow at the soil matrix that is described by Darcy's law and quantified accordingly by the hydraulic conductivity k_f. These four equations describe the response almost completely assuming a linear friction law for the groundwater flow and a linear stress strain behavior of the individual phases.

In the notation of Mei and Foda (1981), the equations are:

$$-\frac{n}{\beta}\frac{\partial p}{\partial t} = \frac{\partial v}{\partial x} + n\frac{\partial (u-v)}{\partial x} \tag{3}$$

$$n\rho_w\frac{\partial u}{\partial t} = -n\frac{\partial p}{\partial x} - \frac{g\cdot\rho_w\cdot n^2}{k_f}(u-v) \tag{4}$$

Fig. 11. Left) Significant wave height with sediment depth for varying tidal phases and water depths. Right) Phase lag observed between subsequent sensors starting with the lag between p_1 and p_2.

$$\frac{\partial \sigma}{\partial t} = E \frac{\partial v}{\partial x} \tag{5}$$

$$(1-n)\rho_s \frac{\partial v}{\partial t} = \frac{\partial \sigma}{\partial x} - (1-n)\frac{\partial p}{\partial x} + \frac{g \cdot \rho_w \cdot n^2}{k_f}(u-v) \tag{6}$$

where ρ_s is the sediment density and ρ_w is the density of the water without the gas. Here σ is the normal stress in the sediment matrix; p is pore water pressure; v is displacement rate of the matrix, u is the displacement rate of the pore water. There are six parameters that describe the systems behavior. The densities of the fluid and solid phase are well known. The parameters porosity n, conductivity after Darcy k_f, Young's modulus of the sediment matrix E and bulk modulus of the water-gas mixture β have to be adjusted. Except for the porosity, the equations are linear.

The compressibility of the fluid phase is that of the combined pore water and gas phases. The bulk modulus of water is 2 GPa. Due to gas bubbles in the pores in the intertidal zone the bulk modulus decreases several orders in magnitude. The combined bulk modulus β of the water and gas phases can be estimated by the formula:

$$\frac{1}{\beta} = \frac{1}{\beta'} + \frac{1-S}{p_0} \tag{7}$$

where S is the gas content and p_0 is the hydrostatic pressure. For a gas content above 1%, the bulk modulus of the liquids is less than that of the sand matrix. For gas contents in the water and gas mixture between 0.1 and 1%, the compressibility of the liquid phase is of the same order as for the sand matrix. Such a small amount of gas may reside in dead end pores in the intertidal zone or result from bioactivity, and the presence of gas was suspected from field measurements as described above.

The relation of the bulk modulus of the liquid phase and sand matrix may change. They may lie in the same range. The interaction of the liquids pressure and the matrix normal stress is however complex. In combination with the horizontal shear stress imposed by the wave orbital motion, the differing normal stress may result in different sediment transport rates (Foda 2003). Moreover, the phase shift of the pressure wave in the vertical direction results in a wave period and wave height dependence of the induced sediment transport following Foda (2003). The hydraulic conductivity k_f of the sediment matrix influences the computation as well. The higher the conductivity the less is the dissipation of energy between the two waves traveling in the column.

Equations (3)–(6) are solved by a simple explicit 1DV finite difference time integration scheme. The variables are solved at a grid with 1 cm resolution. To ensure stability, the time steps are small due to the high velocities of the compression waves in the media and the fine resolution. Using the standard parameters, a time step of 10^{-5} s was small enough to result in a stable time integration for all parameters combinations.

The model was tested using the analytical results for a sinusoidal wave given already by Mei and Foda (1981). The analytical solution for the three-dimensional case was given by Hsu et al. (1993) and Hsu and Jeng (1994). The benefit of using an unsteady 1DV model instead of using the analytical solution is the computation of a time series of real waves instead of using harmonic wave profiles. In the field, the waves transform in shallow water to cnoidal waves. Moreover, the proposition of the model parameters over the vertical direction is flexible. In principle, the model could also account for nonlinearities like the loss of stability of the sediment matrix as proposed by Qi and Gao (2015). However, this extension is not included in the 1DV model at the moment.

In this study, the thickness of the sand layer above the finer moraine layers was found from geologic maps to be about 5 m, and thus, a 5 m long column was modeled. But the results did not differ much for a test computation with a 35 m long column.

The four equations above need two boundary conditions on both ends of the 1DV column. The 1DV column is limited at the seafloor were the wave induced pressure p is described. The matrix stress σ is set to zero at this boundary. At the lower end, the displacement rate of the sediment matrix v and the pore fluid u are commonly set to zero. These conditions are applied in all studies since Mei and Foda (1981). The lower boundary conditions are however a bit ambiguous for the following reasons:

1. No displacement would imply a horizon that does not move at all and is not reacting on the normal stress as the sediment above does.
2. The boundary condition leads to a reflection of the normal stress waves at the lower model end. The pressure waves travel back upwards to the sediment surface where they are again reflected but this time negatively. The resulting resonance is discussed in the literature extensively (Sumer, 2014), but resulted in heavy disturbance in the analysis carried out in this paper.
3. In two-dimensional studies, the normal stress wave can also propagate in the horizontal direction. In the direction of water wave propagation, the stress waves can relax. This should limit the depth of penetration of the pressure wave.
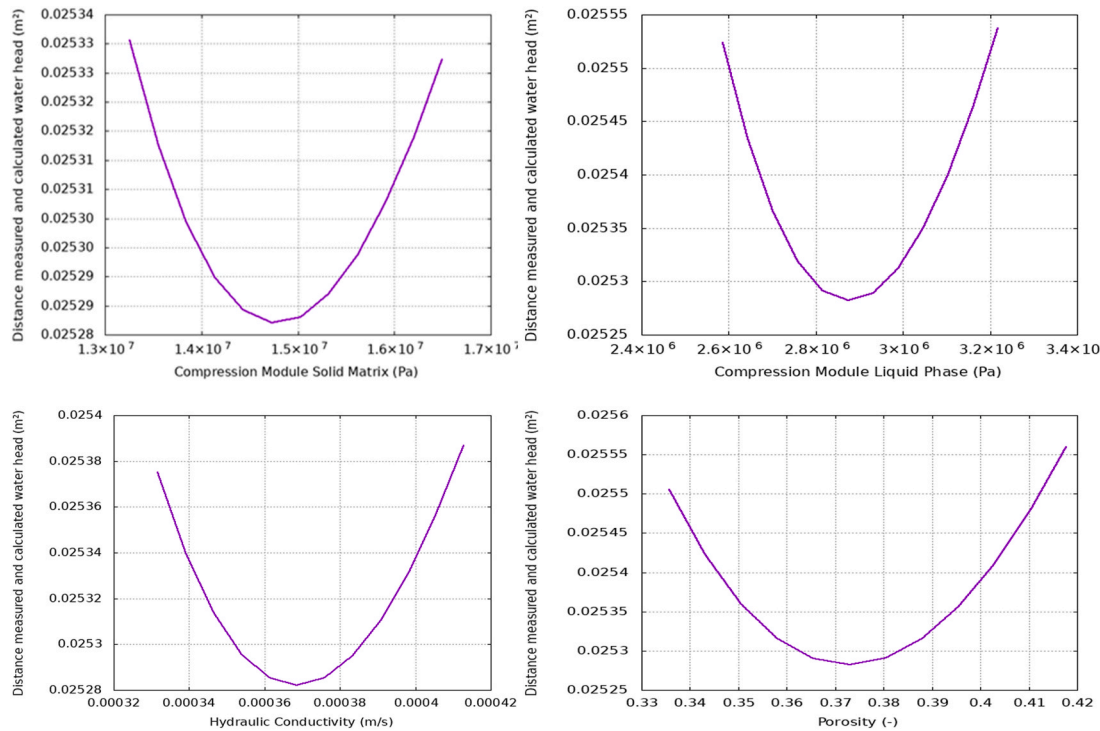
Due to the choice of boundary conditions, resonance may occur in the model. Sumer (2014) investigated this resonance extensively. Resonance occurs in the 1DV column models if the period of the pressure waves induced by the water coincides with the travel time of waves in the combined system. Oscillations with a period of about 0.3 s appeared in the model calculations in the deeper part, where the original water wave pressure changes are already small. The oscillation amplitudes were so large that they influenced the lowest sensor significantly with very short period harmonic oscillations that have not been observed.

The resonance oscillations within the column made the calibration described below impossible because of rapid changes in the goal function (equation (8) below) – the distance between observed and calculated pressures. Therefore, at the lower boundary of the column a dissipative boundary condition was imposed instead of the perfectly reflecting condition of no displacement that has always been used. An exponential damping zone was imposed at the end of the computational domain, like what is done in the field of surface wave modeling. Extremely little damping was necessary to suppress the oscillations in the column that were disturbing the optimization procedure. With these boundary conditions the depth of the modeled column had almost no influence on the computed time series at the pressure sensors anymore.

The time series starts on January the 8th at 21:00. The first 10 s are used to spin the model with a linear ramp factor. After 10 s the statistics are evaluated. The difference between measured (m) and computed (c) pressure values at the three lower sensors were computed over all time steps N with the following root mean square (rms) formula:

$$\varepsilon = \left(\sqrt{\frac{1}{N}\sum_N \left(p_{2,i}^m - p_{2,i}^c\right)^2} + \sqrt{\frac{1}{N}\sum_N \left(p_{3,i}^m - p_{3,i}^c\right)^2} + \sqrt{\frac{1}{N}\sum_N \left(p_{4,i}^m - p_{4,i}^c\right)^2} \right) \Big/ 3 \tag{8}$$

The calibration was carried out by a simple gradient method. Each time one of the four major parameters was changed by a few percent. Then the agreement at the three deeper sensors was compared and the parameter set with the lower difference was kept for the next iteration. A systematic variation of each one of the four system parameters is shown in Fig. 12. Unfortunately, the parameters are not independent. The porosity is a nonlinear factor in equations. A change in porosity changed all other parameters. The bulk modulus is coupled slightly as well. So, increasing the Young's modulus E was followed by an increase of β. At the end, a well-formed optimum was achieved for all parameters as shown in Fig. 12. All parameters have been varied by the same percentage against the optimal values. The remaining rms difference after the calibration averaged over all three sensors was 2.5 cm. The optimal values obtained by this procedure are given in Table 2. The hydraulic

Fig. 12. Dependency of the differences between observed and calculated time series of wave pressure heights in the bed around the optimum for all four soil model parameters: compression module solid matrix, compression module liquid phase, hydraulic conductivity, and porosity.

Table 2
Set of depth uniform parameters in the 1DV model optimized by observed time series.

Parameter	Optimized value
E	13,447,000 Pa
β	2,833,800 Pa
p	0.373
kf	0.0357 cm/s

conductivity is lower than predicted with equation (2) (see Table 1). The bulk modulus of the fluid phase indicates a gas content of about 4%. This value appears feasible considering the local water level variations and observations at other sites. Young's modulus is by a factor of two less than values in the literature. This could be a result of less compaction of the sand. As can be seen in Fig. 12, the influence of the porosity was the largest.

In Fig. 13, the comparison of the computed and the measured pressure time series is shown. The time series corresponds to the first high tide and starts 1 h before the time series shown in Fig. 7. The water depth was 0.7 m. The significant wave height shown in Fig. 2 was 0.5 m during that time and the wind speed about 4 m/s. The hydrostatic pressure has been subtracted and all values are given as meters of water. The amplitude of the measured pressure waves is declining at the deeper transducers. The pressure spikes observed at the uppermost (Fig. 13, top left) sensor are disappearing in the measurements at the deeper sensors. While these spikes are also dampened in the computed pressure signals, they do not dampen as rapidly as the measured pressure signals. Therefore, some spikes are still well observable at the deeper sensors where they combine with artefacts from the resonance wave. The resonance artefacts visible around the time 70 s are still in the computation, because the dissipation at the boundary condition was kept small.
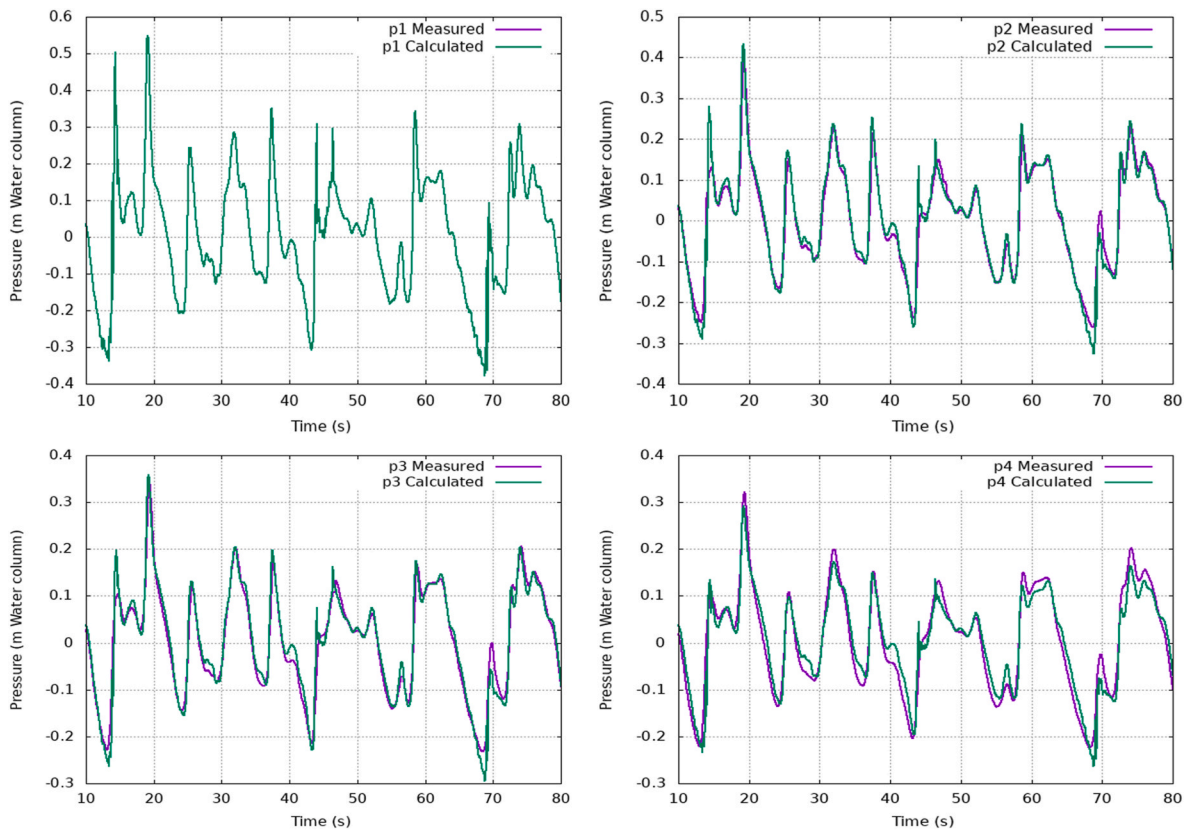
The measured hydraulic gradient time series is shown in Fig. 14 for the same time period. The negative spikes correspond to the wave crests that are shorter and higher for shallow water waves. They may be combined with depth induced wave breaking. The pressure time series at the bed shows wave heights of 0.5 m. The average water depth at high water was about 1 m. It can be concluded that the waves were breaking. For a uniform sediment, the wave induced hydraulic gradient is largest near the sediment surface. This is because the pressure wave is damped with increasing depth, and thus, the gradient is damped. As in Zhai et al. (2021) and in Li et al. (2020) the effect of this hydraulic gradient on incipient sediment motion is important even below the critical gradient. If the critical gradient is exceeded the liquified part of the bed would be diluted, and thus, the hydraulic resistance lowered as described by Qi and Gao (2015). In Fig. 14, the case of momentary liquefaction would be predicted if the critical hydraulic gradient is exceeded that is about 1.0. The critical hydraulic gradient is computed by (1-n) ρ′, with ρ' - the specific gravity of the submerged sediment. This value is beyond the range reached. This suggests that in the present case momentary liquefaction did not occur. Only individual waves exceeded a height of half a meter. On average, the wave height was small. From these values it can be concluded that the waves reduced the weight of the upper sediment layer by about 12 percent at falling water level between wave crest and trough. This could influence sediment transport.
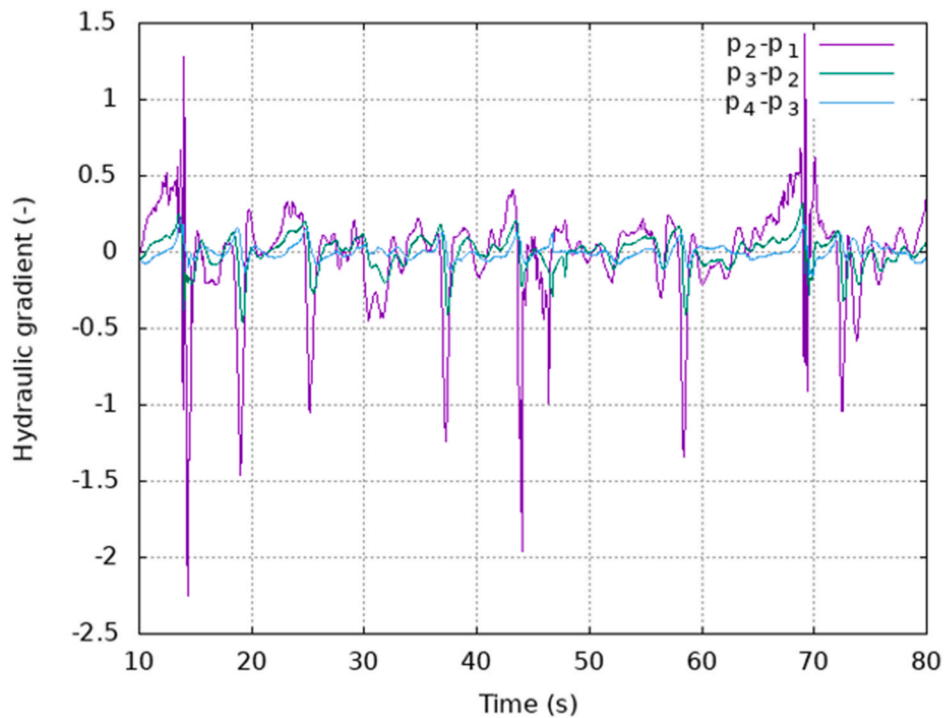
Significant spikes featuring a rapid positive-negative were occasionally identified in the record of p_1 also affecting the gradients as shown in two incidents in Fig. 14. Motion of the sensor could explain this. While it cannot be proven, it can be hypothesized based on the observed exposure and tilting upwards of p_1 that such occasional motion would be a feasible explanation.

5. Conclusions

Two days of field measurements along a cross-shore transect reaching from the foot of the dunes to the upper subtidal zone have been conducted at the western sandy beach of the island of Sylt, Germany, just south of the city of Westerland. Sediment properties and geotechnical parameters were obtained from sediment sampling and limited in-situ testing. Pore pressure measurements were conducted along a vertical array in the upper 55 cm of the beach surface in the lower intertidal zone. Pore pressure recordings were then further analyzed using a 1DV

Fig. 13. Time series of calculated (green lines) and observed (purple lines) pore pressure starting at January 8th at high tide for all four pressure transducers. The uppermost transducer is used as boundary condition for the model. (For interpretation of the references to colour in this figure legend, the reader is referred to the Web version of this article.)

Fig. 14. Time series of measured hydraulic gradient starting at January 8th 21:00. The gradient is computed between the four transducers. Positive gradient is acting upwards.

model based on Biot (1956) and Mei and Foda (1981). The following key observations can be made from the results:

1) Slight trends of increasing grain size and friction angles from the subaerial to the lower intertidal zone were observed based on laboratory testing.

2) In-situ sediment strength testing using a portable free fall penetrometer supported the trends in friction angles for the subaerial and intertidal zone. However, a significant increase in strength was observed in-situ in the swash zone and upper subtidal zone. This observation may support previous hypotheses of beach sand densification by waves in the swash and surf zone.

3) Pore pressure recordings showed a consistent trend associated with the tidal water elevations. However, low tide results suggested a decoupling of surface water effects and groundwater, possibly associated with gas content and negative pore pressures in the vadose zone.

4) Pore pressure recordings suggested a more pronounced wave damping in the upper sediment layers and a minor phase lag between the three deeper sensors. A significant phase shift was associated with the top sensor. While the specific reason for this remains unclear, the tilting and movement of the sensors from being embedded to above the sediment-water interface is likely related.

5) The 1DV pore pressure model succeeded to simulate a chosen excerpt of the pressure time series of observed waves from the site at all sediment depths well, and suggested no liquefaction events during the measurement period, but a reduction of effective weight that may affect sediment dynamics.

This study represents an example of the complexity of geotechnical sediment properties and soil behavior in energetic beach environments. However, the data collection was short and limited to one cross-shore transect. More research is needed to investigate specifically sediment strength in the swash and surf zone, interaction between surface and groundwater processes, as well as pore pressures under wave action.

CRediT authorship contribution statement

Nina Stark: Scientific scope, Data collection, Data analysis, Manuscript development. **Peter Mewis:** Scientific scope, Data collection, Data analysis, Manuscript development. **Bridgit Reeve:** Data collection, Data analysis, Manuscript development. **Matthew Florence:** Data collection, Data analysis, Manuscript development. **Jan Piller:** Data collection, Data analysis. **Jessica Simon:** Data collection, Data analysis.

Declaration of competing interest

The authors declare that they have no known competing financial interests or personal relationships that could have appeared to influence the work reported in this paper.

References

Al-Tarazi, E., 2000. The major Gulf of the Aqaba earthquake, 22 November 1995–Maximum intensity distribution. Nat. Hazards 22 (1), 17–27.

Albatal, A., Stark, N., 2016. In situ geotechnical early site assessment of a proposed wave energy converter site in Yakutat, Alaska, using a portable free-fall penetrometer. Geo-Chicago 429–438.

Albatal, A., Wadman, H., Stark, N., Bilici, C., McNinch, J., 2019. Investigation of spatial and short-term temporal nearshore sandy sediment strength using a portable free fall penetrometer. Coast. Eng. 143, 21–37.

Albatal, A., Stark, N., Castellanos, B., 2020. Estimating in situ relative density and friction angle of nearshore sand from portable free-fall penetrometer tests. Can. Geotech. J. 57 (1), 17–31.

Anwar, J., 1974. Der holozäne Meeressand im Seegebiet westlich von Sylt zwischen Kampen und Rantum (Ausgangsmaterial und Sedimentation). Meyniana 24, 43–55.

Atkins, J.E., McBride, E.F., 1992. Porosity and packing of Holocene river, dune, and beach sands (1). AAPG (Am. Assoc. Pet. Geol.) Bull. 76 (3), 339–355.

Barnes, M.P., O'Donoghue, T., Alsina, J.M., Baldock, T.E., 2009. Direct bed shear stress measurements in bore-driven swash. Coast. Eng. 56 (8), 853–867.

Beyer, W., 1964. Zur Bestimmung der Wasserdurchlässigkeit von Kiesen und Sanden aus der Kornverteilungskurve. WWT 14 (6), 165–168.

Bialas, Z., Kleczkowski, A.S., 1970. O prezdydatnosciniektorych wzorow empirycznych dla okreslenia wspo czynnika filtracji k. Arch. Hydrotech. 407–417.

Biot, M.A., 1956. Theory of propagation of elastic waves in a fluid-saturated porous solid, part I: low frequency range and part 11: higher frequency range. J. Acoust. Soc. Am. 28, 168–191.

Bird, E.C.F., 1996. Beach Management, vol. 5. John Wiley & Son Ltd.

Briaud, J.L., 2013. Geotechnical Engineering: Unsaturated and Saturated Soils. John Wiley & Sons.

BSH, 2017. https://www.bsh.de/DE/DATEN/Seegang/seegang_node.html last accessed January 2017.

Bundeamt fuer Umwelt, 1998. Landesamt für den Nationalpark Schleswig-Holsteinisches Wattenmeer, Umweltbundesamt. In: *Umweltatlas Wattenmeer (Wadden Sea environmental Atlas)* (In German). I – Nordfriesisches und Dithmarscher Wattenmeer, Stuttgart, 1998.

Butt, T., Russell, P., Turner, I., 2001. The influence of swash infiltration–exfiltration on beach face sediment transport: onshore or offshore? Coast. Eng. 42 (1), 35–52.

Cubrinovski, M., Ishihara, K., 2002. Maximum and minimum void ratio characteristics of sands. Soils Found. 42 (6), 65–78.

Dean, R.G., Dalrymple, R.A., 2004. Coastal Processes with Engineering Applications. Cambridge University Press.

Dette, H.H., Raudkivi, A.J., 1995. Beach nourishment and dune protection. In: Coastal Engineering, vol. 1994, pp. 1934–1945.

Fachplan Kuestenschutz Sylt, 2015. Landesamt fuer Kuestenschutz und Natur Schleswig-Holstein.

Foda, M.A., 2003. Role of wave pressure in bedload sediment transport. J. Waterw. Port, Coast. Ocean Eng. 129 (6), 243–249.

Folk, R.L., Ward, W.C., 1957. Brazos River bar [Texas]; a study in the significance of grain size parameters. J. Sediment. Res. 27 (1), 3–26.

Foster, D.L., Bowen, A.J., Holman, R.A., Natoo, P., 2006. Field evidence of pressure gradient induced incipient motion. J. Geophys. Res.: Oceans 111 (C5).

Fuhrböter, A., 1991. Eine theoretische Betrachtung über Sandvorspulungen mit Wiederholungsintervallen. Die Kuste 52, 241–254.

Gallagher, E., Wadman, H., McNinch, J., Reniers, A., Koktas, M., 2016. A conceptual model for spatial grain size variability on the surface of and within beaches. J. Mar. Sci. Eng. 4 (2), 38.

Gori, U., Mari, M., 2001. The correlation between the fractal dimension and internal friction angle of different granular materials. Soils Found. 41 (6), 17–23.

Grabowski, R.C., Droppo, I.G., Wharton, G., 2011. Erodibility of cohesive sediment: the importance of sediment properties. Earth Sci. Rev. 105 (3), 101–120.

Guest, T.B., Hay, A.E., 2017. Vertical structure of pore pressure under surface gravity waves on a steep, megatidal, mixed sand-gravel-cobble beach. J. Geophys. Res.: Oceans 122 (1), 153–170.

Hanson, H., Brampton, A., Capobianco, M., Dette, H.H., Hamm, L., Laustrup, C., Lechuga, A., Spanhoff, R., 2002. Beach nourishment projects, practices, and objectives—a European overview. Coast. Eng. 47 (2), 81–111.

Hazen, A., 1911. Discussions of 'Dams on sand Foundations' by A.C. Koenig. ASCE Trans. 73, 199.

Holman, R.A., Huntley, D.A., Bowen, A.J., 1978. Infragravity waves in storm conditions. In: Coastal Engineering 1978, pp. 268–284.

Horn, D.P., 2002. Beach groundwater dynamics. Geomorphology 48 (1–3), 121–146.

Horn, D.P., 2006. Measurements and modelling of beach groundwater flow in the swash-zone: a review. Continent. Shelf Res. 26 (5), 622–652.

Houser, C., Greenwood, B., 2007. Onshore migration of a swash bar during a storm. J. Coast. Res. 1–14.

Hsu, S.A., 1971. Measurement of shear stress and roughness length on a beach. J. Geophys. Res. 76 (12), 2880–2885.

Hsu, J.R.C., Jeng, D.S., 1994. Wave-induced soil response in an unsaturated anisotropic seabed of finite thickness. Int. J. Numer. Anal. Methods GeoMech. 18 (11), 785–807.

Hsu, J.R.C., Jeng, D.S., Tsai, C.P., 1993. Short-crested wave-induced soil response in a porous seabed of infinite thickness. Int. J. Numer. Anal. Methods GeoMech. 17 (8), 553–576.

Kim, T.H., Sture, S., 2004. Effect of moisture on attraction force in beach sand. Mar. Georesour. Geotechnol. 22 (1–2), 33–47.

Kirchner, J.W., Dietrich, W.E., Iseya, F., Ikeda, H., 1990. The variability of critical shear stress, friction angle, and grain protrusion in water-worked sediments. Sedimentology 37 (4), 647–672.

Kishida, H., 1970. Characteristics of liquefaction of level sandy ground during the Tokachioki earthquake. Soils Found. 10 (2), 103–111.

Lade, P.V., Abelev, A.V., 2003. Effects of cross anisotropy on three-dimensional behavior of sand. II: volume change behavior and failure. J. Eng. Mech. 129 (2), 167–174.

Li, Y., Ong, M.C., Fuhrman, D.R., 2020. CFD investigations of scour beneath a submarine pipeline with the effect of upward seepage. Coast. Eng. 156, 103624.

Lindhorst, S., Betzler, C., Hass, H.C., 2008. The sedimentary architecture of a Holocene barrier spit (Sylt, German Bight): swash-bar accretion and storm erosion. Sediment. Geol. 206 (1), 1–16.

Masselink, G., Hughes, M., Knight, J., 2014. Introduction to Coastal Processes and Geomorphology. Routledge.

Mei, C.C., Foda, M.A., 1981. Wave-induced responses in a fluidfilled poro-elastic solid with a free surface—a boundary layer theory. Geophys. J. Roy. Astron. Soc. 66, 597–637.

Montaño Muñoz, J. K. report*Influence of Infragravity Waves on the Hydrodynamics of Beaches* (Doctoral Dissertation). Universidad Nacional de Colombia-Sede Medellín).

Mory, M., Michallet, H., Bonjean, D., Piedra-Cueva, I., Barnoud, J.M., Foray, P., et al., 2007. A field study of momentary liquefaction caused by waves around a coastal structure. J. Waterw. Port, Coast. Ocean Eng. 133 (1), 28–38.

Nielsen, P., 1992. Coastal Bottom Boundary Layers and Sediment Transport, vol. 4. World Scientific Publishing Co Inc.

Nielsen, P., 2002. Shear stress and sediment transport calculations for swash zone modelling. Coast. Eng. 45 (1), 53–60.

Obermeier, S.F., Weems, R.E., Jacobson, R.B., Gohn, G.S., 1989. Liquefaction evidence for repeated Holocene earthquakes in the coastal region of South Carolina. Ann. N. Y. Acad. Sci. 558 (1), 183–195.

Otto, P., Piter, A., Gijsman, R., 2021. Statistical analysis of beach profiles–A spatiotemporal functional approach. Coast. Eng. 170, 103999.

Pleskachevsky, A., Eppel, D.P., Kapitza, H., 2009. Interaction of waves, currents and tides, and wave-energy impact on the beach area of Sylt Island. Ocean Dynam. 59 (3), 451–461.

Puleo, J.A., Lanckriet, T., Wang, P., 2012. Near bed cross-shore velocity profiles, bed shear stress and friction on the foreshore of a microtidal beach. Coast. Eng. 68, 6–16.

Qi, W.-G., Gao, F.-P., 2015. A modified criterion for wave-induced momentary liquefaction of sandy seabed. Theor. Appl. Mech. Lett. 5, 20–23, 2015.

Raubenheimer, B., Elgar, S., Guza, R.T., 1998. Estimating wave heights from pressure measured in sand bed. J. Waterw. Port, Coast. Ocean Eng. 124 (3), 151–154.

Richter, A., Faust, D., Maas, H.G., 2013. Dune cliff erosion and beach width change at the northern and southern spits of Sylt detected with multi-temporal Lidar. Catena 103, 103–111.

Ruggiero, P., Komar, P.D., McDougal, W.G., Marra, J.J., Beach, R.A., 2001. Wave runup, extreme water levels and the erosion of properties backing beaches. J. Coast Res. 407–419.

Schäffer, H.A., 1993. Infragravity waves induced by short-wave groups. J. Fluid Mech. 247, 551–588.

Sheremet, A., Guza, R.T., Elgar, S., Herbers, T.H.C., 2002. Observations of nearshore infragravity waves: seaward and shoreward propagating components. J. Geophys. Res.: Oceans 107 (C8), 10–11.

Sleath, J.F.A., 1999. Conditions for plug formation in oscillatory flow. Continent. Shelf Res. 19 (13), 1643–1664.

Stark, N., 2016. Geotechnical site investigation in energetic nearshore zones: opportunities and challenges. Aust. GeoMech. 51 (4), 1–7.

Stark, N., Ziotopoulou, K., 2017. Undrained shear strength of offshore sediments from portable free fall penetrometers: theory, field observations and numerical simulations. In: Offshore Site Investigation Geotechnics 8th International Conference Proceeding, vol. 391, pp. 391–399, 399.

Stark, N., Kopf, A., Hanff, H., Stegmann, S., Wilkens, R., 2009. Geotechnical investigations of sandy seafloors using dynamic penetrometers. In: IEEE/MTS OCEANS 2009, pp. 1–10.

Stark, N., Wilkens, R., Ernstsen, V.B., Lambers-Huesmann, M., Stegmann, S., Kopf, A., 2012. Geotechnical properties of sandy seafloors and the consequences for dynamic penetrometer interpretations: quartz sand versus carbonate sand. Geotech. Geol. Eng. 30 (1), 1–14.

Stark, N., Hay, A.E., Cheel, R., Lake, C.B., 2014. The impact of particle shape on the angle of internal friction and the implications for sediment dynamics at a steep, mixed sand-gravel beach. Earth Surf. Dynam. 2 (2), 469–479.

Stark, N., McNinch, J., Wadman, H., Graber, H.C., Albatal, A., Mallas, P.A., 2017. Friction angles at sandy beaches from remote imagery. Géotech. Lett. 7 (4), 292–297.

Steiner, A., Kopf, A.J., L'Heureux, J.S., Kreiter, S., Stegmann, S., Haflidason, H., Moerz, T., 2014. In situ dynamic piezocone penetrometer tests in natural clayey soils—a reappraisal of strain-rate corrections. Can. Geotech. J. 51 (3), 272–288.

Sumer, B.M., 2014. Liquefaction Around Marine Structures:(With CD-ROM). World scientific.

Sumer, B.M., Fredsøe, J., Christiansen, N., 1992. Scour around vertical pile in waves. J. Waterw. Port, Coast. Ocean Eng. 118 (1), 15–31.

Taylor, D., 1948. Fundamentals of Soil Mechanics. John Wiley & Sons, Inc., p. 112

Terzaghi, K., Peck, R.B., 1948. Soil Mechanics in Engineering. John Whiley & Sons, New York.

Tonkin, S., Yeh, H., Kato, F., Sato, S., 2003. Tsunami scour around a cylinder. J. Fluid Mech. 496, 165–192.

Tørum, A., 2007. Wave-induced pore pressures—air/gas content. J. Waterw. Port, Coast. Ocean Eng. 133 (1), 83–86.

Tuller, M., Or, D., 2001. Hydraulic conductivity of variably saturated porous media: film and corner flow in angular pore space. Water Resour. Res. 37 (5), 1257–1276.

Turner, I.L., 1993. Beach face permeability, the groundwater effluent zone, and intertidal profiles of macro-tidal beaches: a conceptual model. In: Catchments and Coasts of Eastern Australia, vol. 5. Department of Geography, University of Sydney, pp. 88–99. Monograph Series.

Turner, I.L., 1998. Monitoring groundwater dynamics in the littoral zone at seasonal, storm, tide and swash frequencies. Coast. Eng. 35 (1–2), 1–16.

Turner, I.L., Masselink, G., 1998. Swash infiltration-exfiltration and sediment transport. J. Geophys. Res.: Oceans 103 (C13), 30813–30824.

Turner, I.L., Nielsen, P., 1997. Rapid water table fluctuations within the beach face: implications for swash zone sediment mobility? Coast. Eng. 32 (1), 45–59.

van der Wal, D., 2000. Grain-size-selective aeolian sand transport on a nourished beach. J. Coast Res. 896–908.

Van Genuchten, M.T., 1980. A closed-form equation for predicting the hydraulic conductivity of unsaturated soils 1. Soil Sci. Soc. Am. J. 44 (5), 892–898.

Van Rijn, L.C., 2007. Unified view of sediment transport by currents and waves. I: initiation of motion, bed roughness, and bed-load transport. J. Hydraul. Eng. 133 (6), 649–667.

Verhagen, H.J., 1993. Method for artificial beach nourishment. In: Coastal Engineering 1992, pp. 2474–2485.

Von Liebermann, Nicole Küstenschutz: *Bisherige und zuküinftige Maßnahmen* (PDF) (in German). Technical University of Harburg. Archived from the original on 11 June 2007.

Wentworth, C.K., 1922. A scale of grade and class terms for clastic sediments. J. Geol. 30 (5), 377–392.

White, D.J., O'Loughlin, C.D., Stark, N., Chow, S.H., 2018. Free fall penetrometer tests in sand: determining the equivalent static resistance. In: Cone Penetration Testing 2018: Proceedings of the 4th International Symposium on Cone Penetration Testing. CRC Press, Boca Raton, FL, USA, pp. 695–701.

Yeh, H., Mason, H.B., 2014. Sediment response to tsunami loading: mechanisms and estimates. Geotechnique 64 (2), 131–143.

Zhai, H., Jeng, D-S., Guo, Z., Liang, Z., 2021. Impact of two-dimensional seepage flow on sediment incipient motion under waves. Appl. Ocean Res. 108, 102510.

Zhang, K., Douglas, B.C., Leatherman, S.P., 2004. Global warming and coastal erosion. Climatic Change 64 (1), 41–58.